International Journal of Nanomedicine

Dovepress
Taylor & Francis Group

Open Access Full Text Article

ORIGINAL RESEARCH

Multifunctional Bismuth Nanoplatforms Augment Radioactive Iodine Therapy in Anaplastic Thyroid Cancer

Xijie Qu[1,2,*], Tong Liu[3,*], Yu Wang[2,4], Xinyuan Wei[2,4], Ye Yang[1], Liya Gu[1], Kun Yang[2], Jing Zhang[1], Yan Liu[1], Yiqian Liang[1], Yanzhen Zheng[2,4], Aimin Yang[1,2]

[1]Department of Nuclear Medicine, The First Affiliated Hospital of Xi'an Jiaotong University, Xi'an, Shaanxi, 710061, People's Republic of China; [2]School of Future Technology, Xi'an Jiaotong University, Xi'an, Shaanxi, 710061, People's Republic of China; [3]Department of Surgical Intensive Care Unit, The First Affiliated Hospital of Xi'an Jiaotong University, Xi'an, Shaanxi, 710061, People's Republic of China; [4]Frontier Institute of Science and Technology, Xi'an Jiaotong University, Xi'an, Shaanxi, 710054, People's Republic of China

*These authors contributed equally to this work

Correspondence: Aimin Yang, Department of Nuclear Medicine, The First Affiliated Hospital of Xi'an Jiaotong University, 277 West Yanta Road, Xi'an, Shaanxi, 710061, People's Republic of China, Email yangaimin@mail.xjtu.edu.cn; Yanzhen Zheng, Frontier Institute of Science and Technology, Xi'an Jiaotong University, 99 Yanxiang Road, Xi'an, Shaanxi, 710054, People's Republic of China, Email zheng.yanzhen@xjtu.edu.cn

Introduction: Radioactive iodine (RAI) therapy is a highly specific targeted treatment for thyroid cancer. However, the intrinsic low energy of ^{131}I limits its efficacy in tumor eradication. Additionally, certain thyroid cancers exhibit a loss of sodium/iodine symporter (NIS) function due to severe dedifferentiation, compromising the therapeutic effectiveness of RAI.

Methods: Our work was based on two distinct RAI-sensitizing strategies: (1) the generation of secondary electrons by irradiated metallic nanomaterials to promote hydrolysis and enhance reactive oxygen species (ROS) production, and (2) drug-induced reversal of the dedifferentiated phenotype of tumor cells to restore iodine uptake. Accordingly, we developed a multifunctional nanoplatform, termed Bi@Digoxin, by loading digoxin onto bismuth nanoparticles (BiNPs). The physicochemical properties of Bi@Digoxin were systematically characterized. Furthermore, its therapeutic efficacy was rigorously evaluated through in vitro and in vivo experiments, demonstrating significant treatment outcomes.

Results: The experiments demonstrate that Bi@Digoxin enhances the efficacy of RAI in Anaplastic thyroid cancer (ATC) through a triple synergistic mechanism: utilizing nanocarriers for efficient delivery of Digoxin to restore NIS function in tumor cells, reversing RAI resistance in ATC; leveraging the high atomic number property of bismuth (Bi) to enhance radiation energy deposition, promoting ROS bursts and DNA double-strand breaks; and combining near-infrared (NIR) laser-triggered controlled drug release with photothermal ablation to significantly inhibit tumor growth.

Conclusion: Bi@Digoxin significantly enhances the therapeutic efficacy of RAI, offering a novel synergistic treatment strategy for ATC that combines biosafety and scalable production, with significant potential for clinical translation.

Keywords: radioactive iodine, redifferentiation, radiosensitization, photothermal therapy

Introduction

Anaplastic thyroid cancer (ATC) represents a rare yet highly malignant subtype of thyroid carcinoma, characterized by a particularly poor prognosis.[1] Predominantly affecting elderly individuals, ATC exhibits a higher prevalence in female patients.[2] The median overall survival (OS) for individuals diagnosed with ATC is approximately 5 months, with a one-year OS rate of 20% and a disease-specific mortality rate approaching 100%.[3] The aggressive nature of ATC often results in its diagnosis at an advanced, inoperable stage, where systemic chemotherapy demonstrates limited efficacy.[4] In the context of differentiated thyroid cancer, Radioactive iodine (RAI) therapy plays a critical role. The decay of ^{131}I emits β-rays, which directly damage the DNA of residual thyroid tissues and cancer cells,[5] inducing apoptosis and facilitating the elimination of

https://doi.org/10.2147/IJN.S561413
Received: 18 August 2025
Accepted: 6 January 2026
Published: 13 January 2026

postoperative residual thyroid tissues as well as the treatment of metastatic lesions.[6] However, in ATC, the functional expression of the sodium/iodine symporter (NIS) on the cell membrane is lost due to cellular dedifferentiation,[7] rendering the tumor resistant to RAI therapy.[8] Additionally, the relatively low energy of ^{131}I (max.0.6065 MeV) contributes to suboptimal therapeutic efficacy.[9] To effectively reengage ^{131}I in anaplastic thyroid carcinoma (ATC), it is essential not only to restore functional NIS expression on the tumor cell membrane to facilitate iodide uptake but also to employ a combination of other therapeutic strategies.

Digoxin emerges as a promising adjuvant therapy for enhancing iodide affinity in thyroid cancer cells.[10] By inhibiting Na/K ATPase, digoxin markedly restores functional NIS expression and enhances iodide uptake in ATC cell lines.[11] However, the narrow therapeutic index of digoxin poses a challenge, as the concentration required for redifferentiation surpasses the maximum tolerated dose.[12] Moreover, no studies have yet optimized the digoxin dosage necessary to restore functional NIS in ATC effectively. Nanomedicine offers a solution to the issue of limited drug bioavailability by enabling the passive or active delivery of substantial quantities of hydrophobic drugs directly to the tumor site.[13] This nanoparticle-mediated drug delivery approach has the potential to profoundly improve the safety and efficacy of anticancer therapeutic agents.[14] In the biomedical domain, bismuth (Bi) compounds have been employed clinically for over three centuries as medications administered at relatively high dosages.[15] These compounds are metabolized through urinary excretion facilitated by metallothionein,[16] resulting in an in vivo biosafety profile that surpasses that of other heavy-metal-based nanoreagents. The high atomic number of Bi (Z = 83) renders it an effective sensitizer for radiotherapy,[17] as its interaction with radiation can produce a substantial number of secondary electrons. This interaction promotes hydrolysis and enhances the generation of reactive oxygen species (ROS), thereby augmenting the DNA-damaging capacity against tumor cells.[18] Furthermore, Bi-based nanomaterials exhibit strong light absorption in the near-infrared (NIR) region and possess excellent photothermal conversion properties, which hold remarkable potential for applications in the photothermal therapy (PTT) of tumors.[19]

In this study, a new therapeutic platform is proposed to synthesize bismuth nanoparticles (BiNPs) using glucose as surfactant and then load digoxin by simple physical agitation to obtain Bi@Digoxin (Scheme 1). The glucose modification exploits the elevated glucose uptake by tumors to facilitate higher drug accumulation.[20] The platform aims to better restore the iodine uptake capacity of tumor cells, and to improve RAI therapy by combining radiosensitization and PTT. Upon administration of Bi@Digoxin at the tumor site, a thermoresponsive release of the drug, coupled with photothermal treatment, is achieved through NIR irradiation. This process upregulates the expression of the NIS in tumor cells. Furthermore, the interaction between radiation and BiNPs enhances ROS production, leading to an increased incidence of DNA double-strand breaks (DSBs) (Scheme 2). Consequently, Bi@Digoxin markedly enhanced the efficacy of RAI in ATC by restoring iodine uptake, increasing sensitivity to radiotherapy, and integrating with PTT.

Results and Discussion

Synthesis and Characterization

We employed a chemical reduction technique to synthesize glucose-modified Bi metal nanoparticles, which concurrently serves to protect the BiNPs' surface from oxidative decomposition in aqueous environments. The morphology of the synthesized BiNPs was characterized using TEM. The TEM analysis revealed that the BiNPs exhibited irregular, faceted morphologies with an average particle size of ~70 nm (Figure 1A). In addition to the C and O signals originating from the sample substrate, the EDS analysis exclusively revealed prominent peaks corresponding to the Bi element (Figure 1B and C). High-resolution TEM imaging further indicated a lattice spacing of ~0.33 nm, corresponding to the (012) plane of Bi single crystals (Figure 1D). XRD analysis

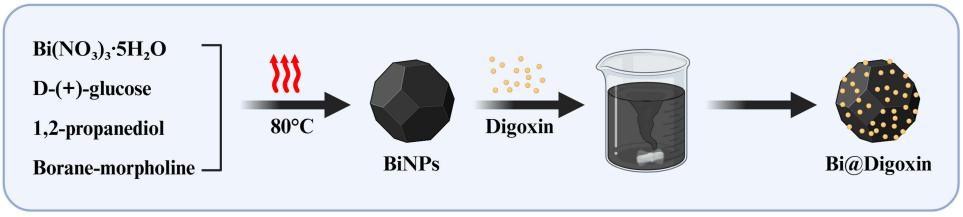

Scheme 1 Synthesis Schematic of Bi@Digoxin.

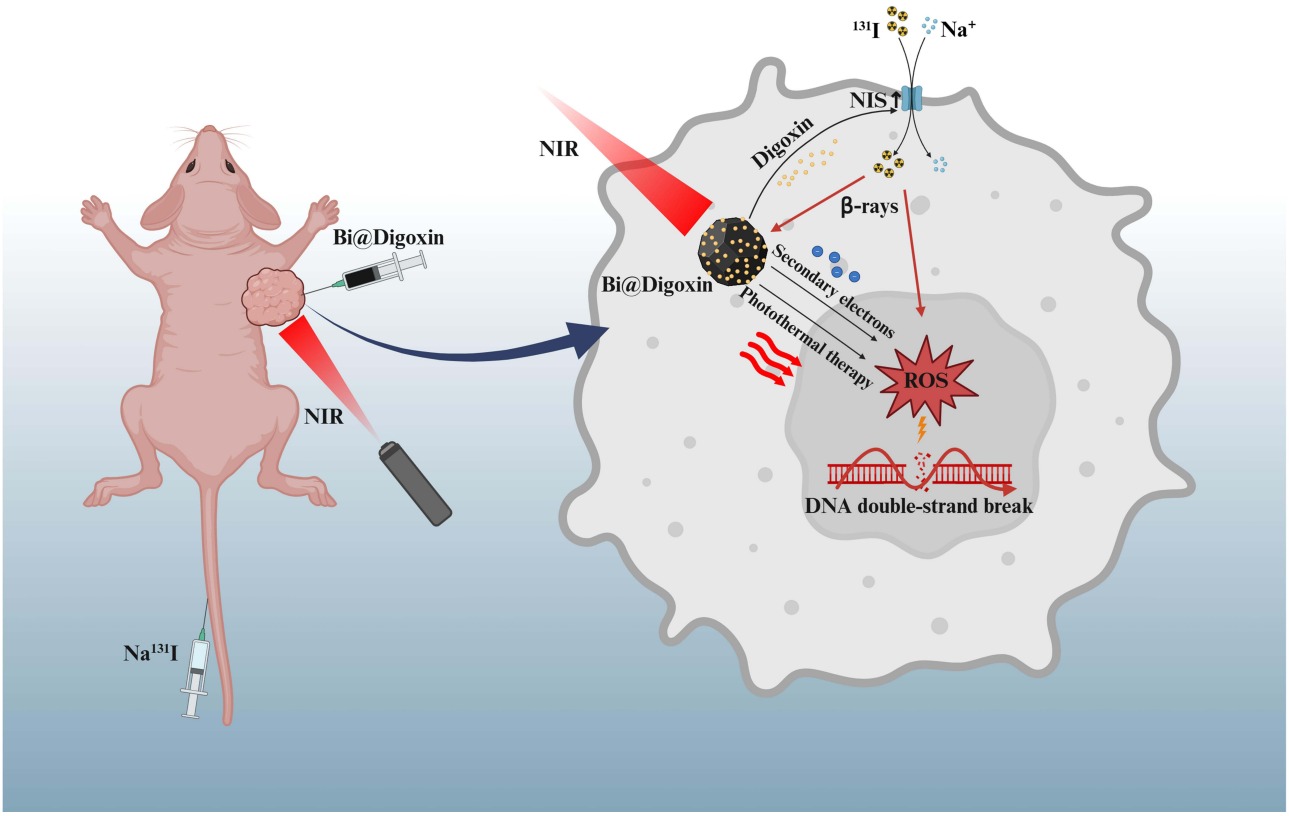

Scheme 2 Schematic illustration of the mechanism by which Bi@Digoxin enhances the efficacy of RAI therapy in tumors.

confirmed that all diffraction peaks of the BiNPs samples were in perfect alignment with the hexagonal phase of Bi (PDF#85-1329), suggesting excellent crystallinity and high sample purity (Figure 1E). The FT-IR spectra revealed characteristic features of surfactants, with a broad IR absorbance observed between 1000 and 1100 cm^{-1}, which can be attributed to C-O and C-C bonds, closely resembling the glucose standard (Figure 1F). As a result of the application of an organic surface stabilization coating, the average hydrodynamic diameter experienced a modest increase, reaching 100 nm (Figure 1G).

Bi@Digoxin Exhibit NIR-Triggered Drug Release

The photothermal characteristics of BiNPs are depicted in Figure 2A and B. BiNPs were dispersed in deionized water at varying concentrations of 0, 10, 20, 40, 100, and 200 μg/mL. These suspensions were subjected to irradiation with a NIR laser (808 nm, 1W) for a duration of 10 minutes, with the system temperature being recorded at one-second intervals. The results demonstrated a significant increase in the temperature of the BiNPs suspension under laser irradiation, correlating positively with both the concentration of BiNPs and the duration of irradiation, while the control sample (deionized water) exhibited negligible temperature change. To evaluate the drug loading capacity of BiNPs, the absorbance standard curve of digoxin was measured utilizing a UV-Vis-NIR (Figure 2C). Digoxin molecules were adsorbed onto the BiNPs through a straightforward mixing and stirring process, denoted as Bi@Digoxin. The experiments examined the impact of varying the initial mass of Digoxin on the drug loading capacity of the BiNPs. It was observed that while the drug loading capacity increased with higher amounts of Digoxin, the drug loading efficiency showed a gradual decline (Figure 2D and E). Following a thorough evaluation of the loading capacity and efficiency, Bi@Digoxin, with an approximate loading amount of 14.7% and a mass ratio of Digoxin to BiNPs of 1:1, was selected for subsequent experimental procedures. UV-Vis-NIR absorption spectroscopy confirmed the successful loading of Digoxin, as evidenced by the presence of its characteristic absorption peaks in Bi@Digoxin, in contrast to those of

https://doi.org/10.2147/IJN.S561413

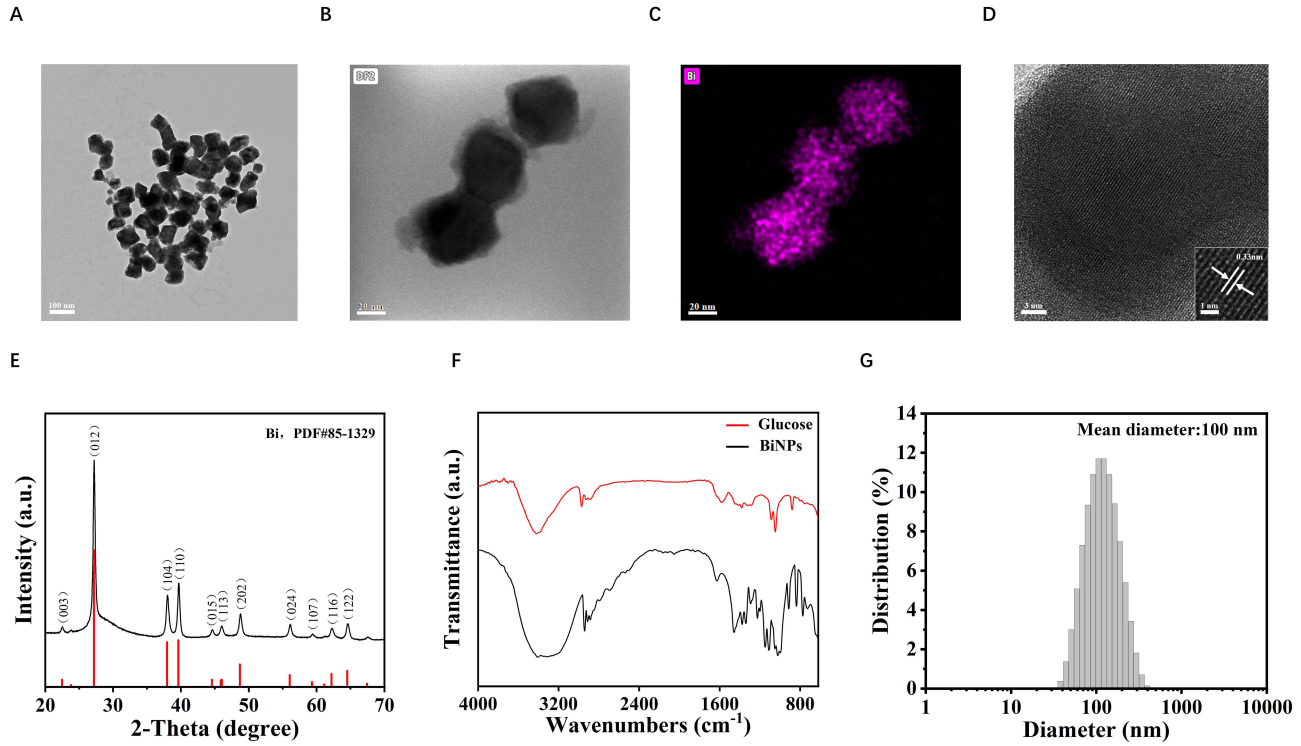

Figure 1 (**A**) Representative TEM image. (**B**) EDS morphology image. (**C**) EDS elemental mapping image. (**D**) HRTEM of the BiNPs (Arrows: Lattice Spacing). (**E**) XRD analysis. (**F**) FT-IR spectroscopy. (**G**) The diameter distribution histogram of the BiNPs.

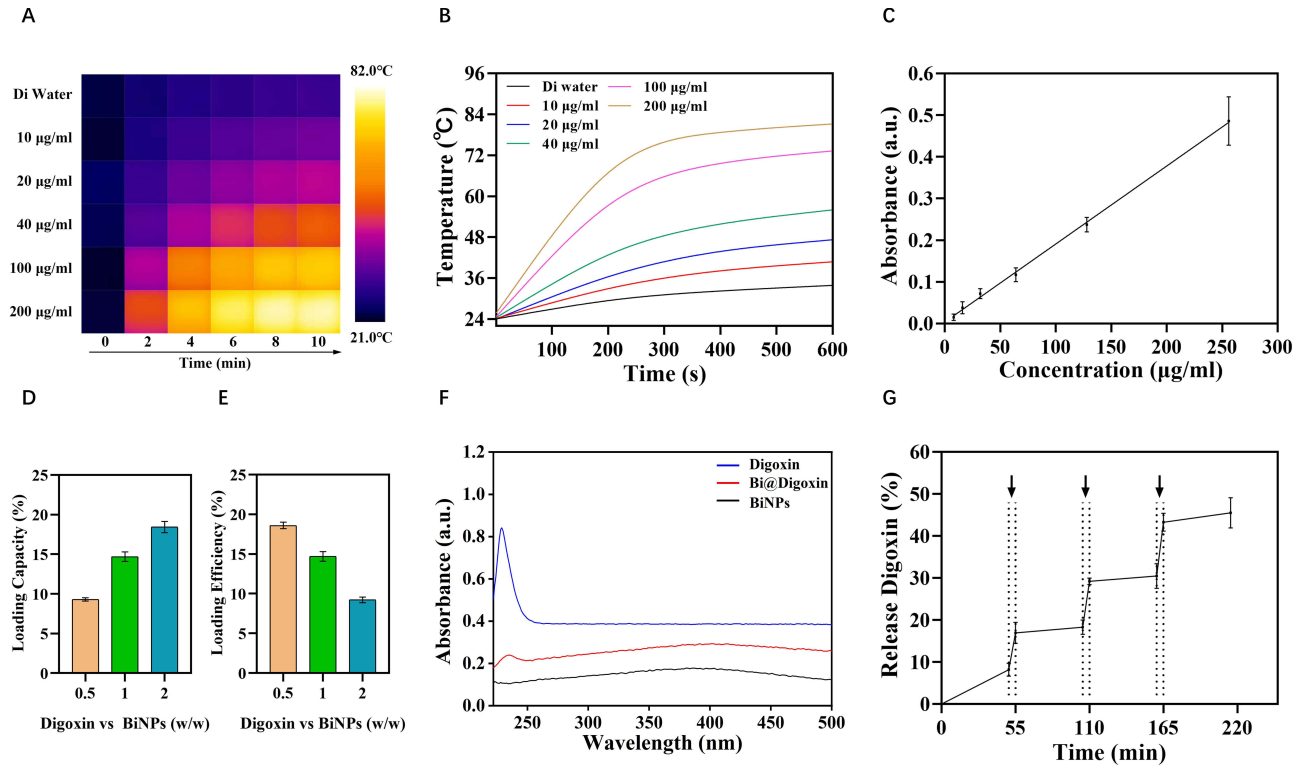

Figure 2 (**A**) Infrared thermography of BiNPs suspensions with different concentrations over time under NIR irradiation (808 nm, 1 W). (**B**) Temperature changes of BiNPs suspensions with different concentrations over time under NIR irradiation (808 nm, 1 W). (**C**) Absorbance standard curve of Digoxin. (**D**) The effect of adding different masses of initial Digoxin on the drug loading capacity of BiNPs. (**E**) The effect of adding different masses of initial Digoxin on the drug loading efficiency of BiNPs. (**F**) Comparison of absorbance curves before and after loading of BiNPs with Digoxin. (**G**) Bi@Digoxin drug release profile with the arrow pointing to the laser irradiation time period (808 nm, 1 W, 5 min). Data are shown as mean ± SD. (n = 3).

https://doi.org/10.2147/IJN.S561413

BiNPs alone (Figure 2F). Alterations in zeta potential provide further corroboration for this outcome (Figure S1 and Supporting Information). Further investigation into the thermoresponsive drug release capability of Bi@Digoxin was conducted using the standard curve of Digoxin. Upon laser irradiation, a rapid release of the drug was observed, which subsequently decreased once the laser was turned off (Figure 2G). This thermoresponsive drug release characteristic holds promising potential for controlled drug delivery applications targeting tumor sites.[21]

Bi@Digoxin Boosts Tumor RAI Therapy via NIS Restoration and Photothermal Synergy

The viability of HUVEC and 8505C cells following co-culture with varying concentrations of BiNPs suspensions was assessed using the CCK-8 assay. As depicted in Figure 3A, BiNPs exhibited no significant impact on the viability of HUVEC cells. In contrast, a reduction in viability was observed in 8505C cells at elevated concentrations, potentially attributable to differential uptake rates. To ensure biological safety, a concentration of 10 μg/mL was selected for subsequent biological validation experiments. The optimal dose of ^{131}I was determined through CCK-8 assays. Upon co-culturing 8505C cells with varying concentrations of ^{131}I, it was observed that the concurrent application of BiNPs (10 μg/mL) led to a further reduction in cell viability compared to treatment with ^{131}I alone (Figure 3B). These findings tentatively indicate that BiNPs may enhance the efficacy of RAI therapy, and a concentration of 400 μCi/mL was chosen for ^{131}I in subsequent cellular experimental studies based on the CCK-8 assay results. In our investigation of the effects of Digoxin and Bi@Digoxin on cell viability, we determined that there was no significant impact on cell viability across the range of drug concentrations utilized in the experiment. This finding corroborates the safety and appropriateness of the selected dosage (Figure 3C).

To ascertain the differential uptake of glucose-modified BiNPs between normal and tumor cells, we employed BioTEM to visualize the internalization of BiNPs within the cytoplasm of both HUVEC and 8505C cells. Our observations revealed a significantly higher accumulation of BiNPs in 8505C cells compared to HUVEC cells (Figure 3D). This finding was corroborated by quantitative analysis using ICP-MS, which demonstrated that, at 8 hours post-exposure, the uptake of the Bi element in HUVEC cells was ~21 ng/10^5 cells, whereas in 8505C cells, it was ~34 ng/10^5 cells—an increase of about 1.6-fold (Figure 3E). These results indicate a differential uptake of BiNPs between normal and tumor cells, highlighting the efficacy of glucose modification as a strategy for targeted delivery. Additionally, it is noteworthy that thyroid cells serve as the primary iodine reservoirs in the body, with their iodine uptake capacity being predominantly regulated by the NIS located in thyroid follicular cells. This symporter facilitates the uptake of iodide ions against the electrochemical gradient, driven by the sodium gradient generated through the sodium-potassium pump exchange mechanism.[22] To further ascertain whether BiNPs enhance the delivery of Digoxin to cells and thereby augment the differentiation rate, we assessed the expression of NIS across various experimental groups. Compared to the group treated with free Digoxin, a notable enhancement in the redifferentiation effect was observed when Digoxin was delivered via BiNPs (Figure 3F and G). Additionally, the expression of Cleaved PARP was evaluated in each group to monitor cellular apoptosis under different treatment conditions. The group treated with ^{131}I + BiNPs + NIR exhibited the highest Cleaved PARP expression among all experimental groups, whereas the group treated with ^{131}I alone demonstrated the lowest Cleaved PARP expression, with no expression detected in the control and BiNPs culture groups (Figure 3F and G). These findings further corroborate the effective sensitization of BiNPs to RAI therapy, and suggest that supplementary PTT can significantly enhance tumor cell eradication. Caspase-3/7 activity assay further confirmed this result (Figure 3H).

To investigate whether RAI accumulation increased concomitantly with the upregulation of NIS function, we conducted ^{125}I uptake assays. In our study, treatments with Digoxin and Bi@Digoxin led to varying degrees of enhanced iodine uptake capacity in 8505C cells. To elucidate the relationship between increased iodine uptake and drug-mediated NIS function, we conducted inhibition studies using $NaClO_4$, a specific inhibitor of the NIS.[23] It is noteworthy that the Bi@Digoxin treatment group exhibited the most significant correlation (Figure 3I). These findings indicate that the Bi@Digoxin treatment enhances the functional expression of NIS proteins, thereby augmenting iodine uptake in 8505C cells. In addition, we employed the same experimental approach to compare the redifferentiation effects of Bi@Digoxin with those of the pioneering drug in redifferentiation therapy, the small-molecule MEK1 and MEK2 inhibitor selumetinib, on 8505C cells. At conventional doses, Bi@Digoxin still demonstrated superior redifferentiation efficacy (Figure S2 and Supporting Information). Subsequently, we investigated the tumoricidal effects of the combination treatment through live-dead cell staining. The results revealed that cells subjected to the combination treatment exhibited a marked and progressive increase in red fluorescence intensity relative to the control group, thereby confirming the cytotoxic impact of the BiNPs combination treatment platform on the cells (Figure 3J).

https://doi.org/10.2147/IJN.S561413

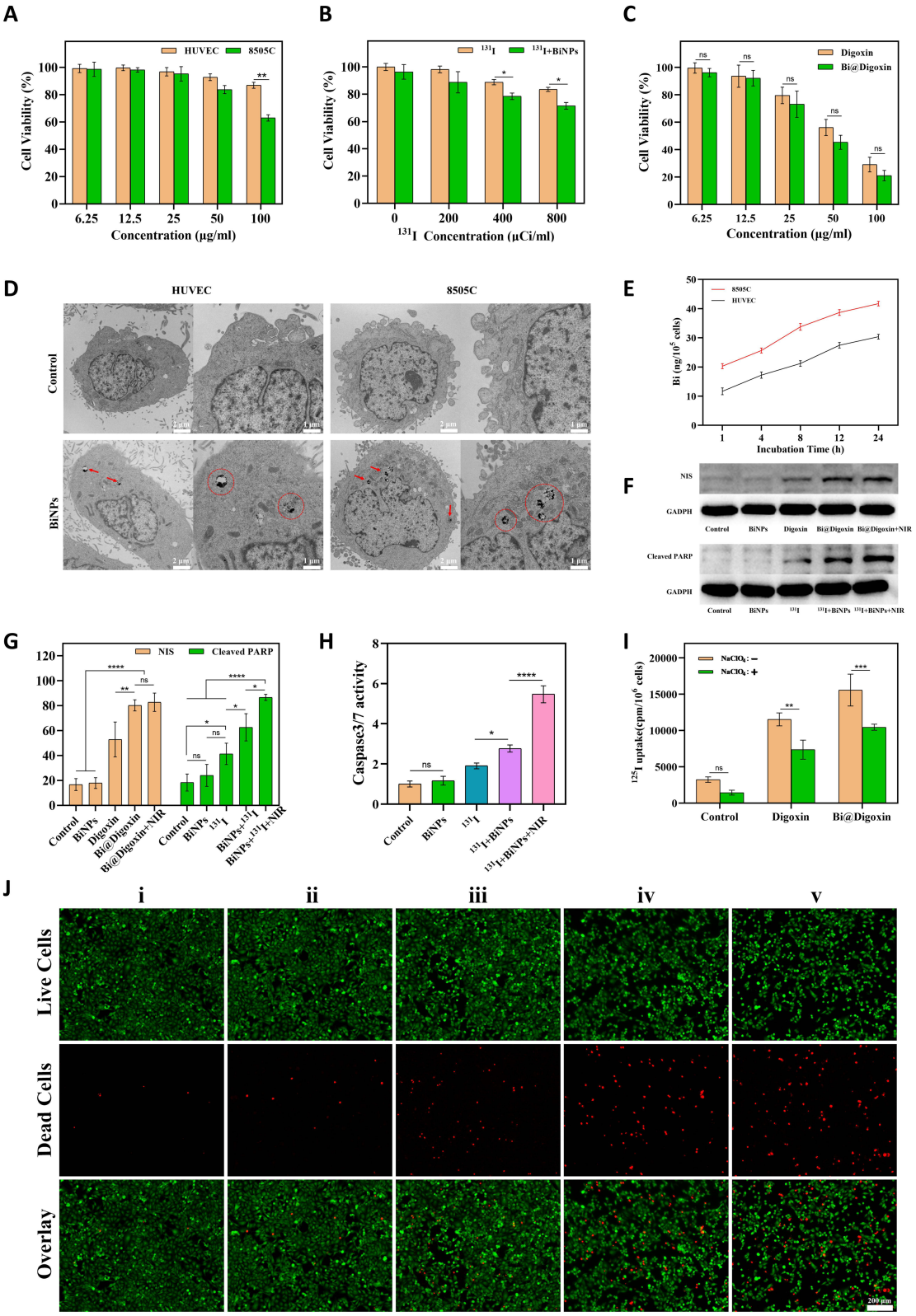

Figure 3 Comprehensive assessment of biocompatibility, radiosensitizing ability, and efficacy of combination therapy with BiNPs. (**A**) Cell viability of HUVEC and 8505C cells treated with BiNPs at gradient concentrations for 24 h. (**B**) Cell viability of 8505C cells co-treated with different concentrations of ^{131}I and BiNPs for 24 h. (**C**) Cell viability of 8505C cells treated with gradient concentrations of Digoxin and Bi@Digoxin. (**D**) TEM images of HUVEC and 8505C cells incubated with or without BiNPs for 4 h (Arrows: Cellular uptake of BiNPs. Circle: Magnified view of intracellular BiNPs). (**E**) Quantification of cellular uptake of BiNPs after incubation with cells for different time periods by ICP-MS. (**F**) Expression of NIS, Cleaved PARP in different treatment groups of 8505C cells. (**G**) Quantification of NIS, Cleaved PARP in different treatment groups of 8505C cells. (**H**) Caspase-3/7 activity in different treatment groups of 8505C cells. (**I**) Quantification of iodine uptake in different treatment groups of 8505C cells. (**J**) Staining of live and dead cells in different treatment groups of 8505C cells. i: Control; ii: ^{131}I; iii: ^{131}I + BiNPs; iv: ^{131}I + Bi@Digoxin; v: ^{131}I + Bi@Digoxin + NIR. Data are shown as mean ± SD. (n = 3), ns (not significant), *p < 0.05, **p < 0.01, ***p < 0.001, ****p < 0.0001.

https://doi.org/10.2147/IJN.S561413

Bi@Digoxin Combination Therapy Suppresses Tumor Proliferation via ROS-Mediated DSBs

Ionizing radiation and thermal stress contribute to the accumulation of ROS through mechanisms including direct damage by energetic particles and protein denaturation, respectively.[24,25] This accumulation subsequently impacts the functional integrity and viability of cells.[26] To assess changes in ROS levels, the fluorescence intensity of the DCFH-DA probe was measured by monitoring the cells. Cells treated solely with ^{131}I exhibited weak green fluorescence. In contrast, the group subjected to combination treatment demonstrated a progressive enhancement in fluorescence intensity (Figure 4A and B), indicating a substantially higher production of ROS compared to RAI therapy alone. Given that DNA is a critical target of ROS and that DSBs represent the most severe form of cellular damage induced by ROS,[27] we further investigated alterations in DSBs. This was achieved by detecting the formation of γ-H2AX through immunofluorescence assays to assess DNA damage. Through a comparative analysis of fluorescence images across different treatment groups, it was observed that the number of γ-H2AX foci increased proportionally with the escalation of treatment modalities. This finding indicates that all components of the nano drug delivery system were effectively sensitized to RAI therapy, resulting in a pronounced elevation in the incidence of DSBs in 8505C cells (Figure 4C and D). The heightened occurrence of DSBs is associated with the inhibition of cell proliferation.[28] To investigate this phenomenon, a cell cloning assay was conducted to assess the long-term impact of each treatment group on the proliferation of 8505C cells. The results revealed that the group treated with ^{131}I + Bi@Digoxin + NIR exhibited the lowest colony formation rate and survival fraction (Figure 4E–G). These findings demonstrate that the Bi@Digoxin combination treatment platform effectively enhances the rate of DSBs in tumor cells through the generation of ROS, thereby leading to sustained inhibition of cell proliferation.

In vivo Toxicology of BiNPs

We conducted an investigation into the in vivo toxicity of BiNPs by analyzing alterations in blood indices between control and BiNP-treated mice. At two weeks post-injection, assessments of liver function indices, including blood alanine aminotransferase (ALT), aspartate aminotransferase (AST), and alkaline phosphatase (ALP) levels, as well as renal function indices such as uric acid (UA) and blood urea nitrogen (BUN) levels, remained within normal physiological ranges.[29] This observation suggests that the hepatic and renal functions were not adversely impacted by BiNP exposure (Figure S3 and Supporting Information). Furthermore, no significant deviations were observed in other blood indices when compared to the control group (Figure S4 and Supporting Information). Histological examination of major organs, including the heart, liver, spleen, lungs, and kidneys, revealed no discernible morphological alterations in mice administered with BiNPs (Figure S5 and Supporting Information). Additionally, the hemolysis rate following BiNP treatment was less than 5% relative to deionized water, indicating favorable blood compatibility, with no significant hemolysis detected even at elevated concentrations (Figure S6 and Supporting Information). We investigated the changes in BiNPs concentration in the bloodstream and their distribution in mice (Figure S7 and Supporting Information). BiNPs exhibited prolonged circulation time in the mouse blood system. The highest concentrations of BiNPs were found in the liver and spleen, indicating their uptake and metabolism by the mononuclear phagocyte system of the body. Additionally, elevated levels of Bi were detected in the kidney tissues of the mice, suggesting that a portion of BiNPs is also metabolized in the kidneys.

Bi@Digoxin Combination Therapy Suppresses Tumor Growth and Upregulates NIS in vivo

The synergistic effect of the Bi@Digoxin combination therapy platform in conjunction with RAI therapy was systematically investigated for the first time. Mice with tumor volumes of approximately 100 mm^3 were allocated into five treatment groups: Control, ^{131}I, ^{131}I + BiNPs, ^{131}I + Bi@Digoxin, and ^{131}I + Bi@Digoxin + NIR. After 14 days, the average tumor volumes in the Control and ^{131}I treatment groups increased to 769 mm^3 and 548 mm^3, respectively. In contrast, the mean tumor volumes in the ^{131}I + BiNPs and ^{131}I + Bi@Digoxin treatment groups increased to 371 mm^3 and 295 mm^3, respectively. Notably, the ^{131}I + Bi@Digoxin + NIR combination treatment group exhibited a marked suppression of tumor growth, with the mean tumor volume reduced to approximately 109 mm^3 (Figure 5A and B). Tumor weight is as shown in Figure 5C. Throughout the observation period, no marked fluctuations in body weight or signs of malignancy were observed, indicating the biosafety of the formulated treatment (Figure 5D). The experimental results demonstrated that the ^{131}I + Bi@Digoxin + NIR combination

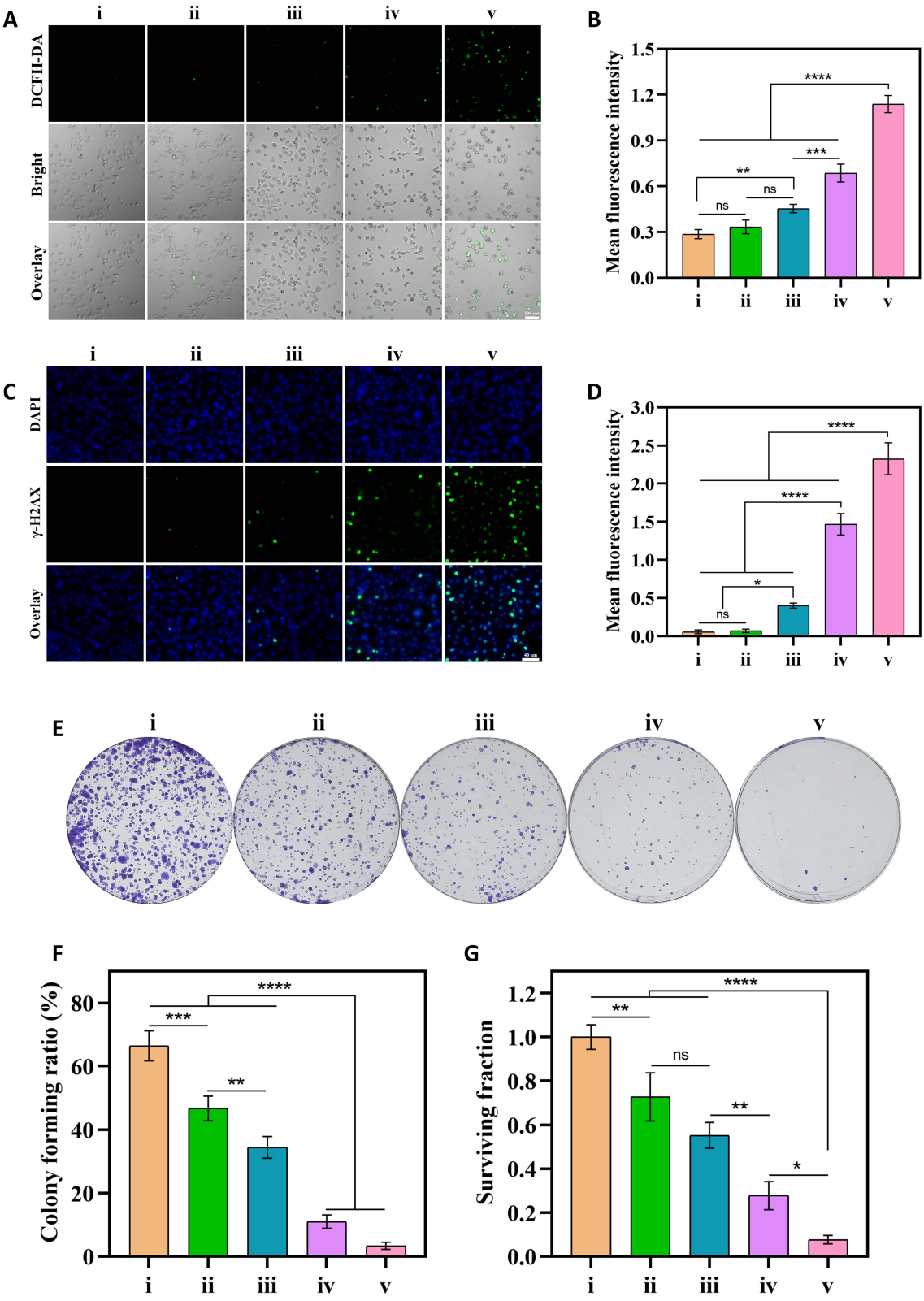

Figure 4 Combination therapy mechanism explored. (**A**) Fluorescence images of ROS in different treatment groups. (**B**) Quantification of ROS in different treatment groups. (**C**) Fluorescence images of γ-H2AX in different treatment groups. (**D**) Quantification of γ-H2AX in different treatment groups. (**E**) Colony formation images in different treatment groups. (**F**) Colony forming ratio in different treatment groups. (**G**) Surviving fraction in different treatment groups. i: Control; ii: ^{131}I; iii: ^{131}I + BiNPs; iv: ^{131}I + Bi@Digoxin; v: ^{131}I + Bi@Digoxin + NIR. Data are shown as mean ± SD. (n = 3), ns (not significant), *p < 0.05, **p < 0.01, ***p < 0.001, ****p < 0.0001.

https://doi.org/10.2147/IJN.S561413

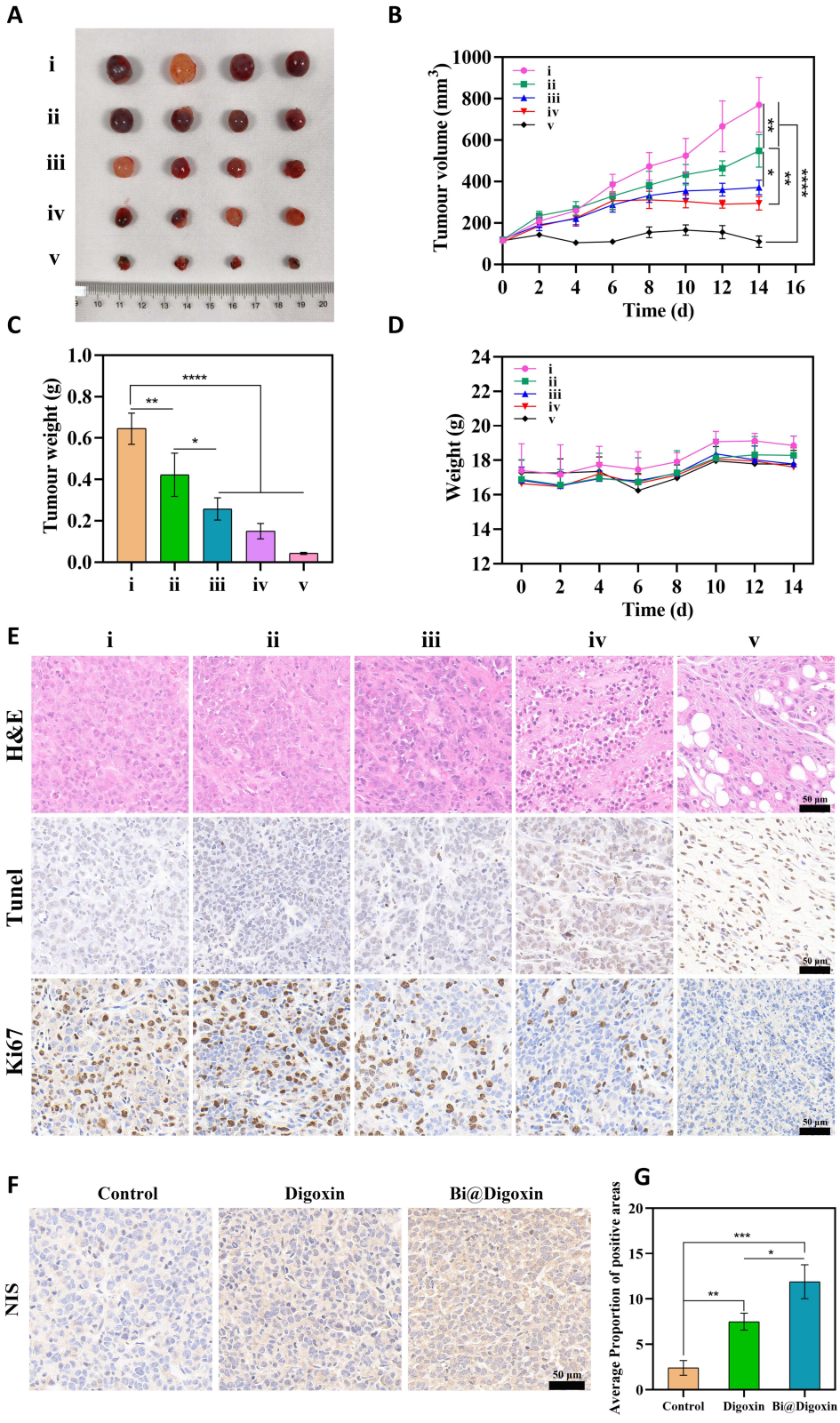

Figure 5 In vivo efficacy assessment of combination therapy. (**A**) Images of tumors after 14 days in different treatment groups. (**B**) Tumor volume changes within 14 days in different treatment groups. (**C**) Tumor weights after 14 days in different treatment groups. (**D**) Body weight changes within 14 days in different treatment groups. (**E**) Tumor tissues in H&E staining, TUNEL staining, and Ki 67 staining. (**F**) Tumor tissues in different treatment groups NIS staining. (**G**) Tumor tissues in different treatment groups NIS quantification. i: Control; ii: ^{131}I; iii: ^{131}I + BiNPs; iv: ^{131}I + Bi@Digoxin; v: ^{131}I + Bi@Digoxin + NIR. Data are shown as mean ± SD. (n = 4), *p < 0.05, **p < 0.01, ***p < 0.001, ****p < 0.0001.

https://doi.org/10.2147/IJN.S561413

exhibited the most effective therapeutic outcome. To further investigate the anti-tumor efficacy of the combination therapy, we collected tumor tissues and conducted H&E staining, TUNEL assay, and Ki-67 immunohistochemical staining (Figure 5E). The histological analysis revealed a pronounced reduction in tumor cell density in the combination treatment group. TUNEL staining indicated a marked increase in apoptotic cells, while Ki-67 staining demonstrated the lowest proliferative capacity in cells subjected to the combination treatment. Additionally, we examined changes in NIS expression in tumors from nude mice by establishing Control, Digoxin, and Bi@Digoxin treatment groups. As illustrated in Figure 5F and G, the expression of NIS protein was markedly elevated in the Bi@Digoxin treatment group compared to the other groups. These findings suggest that the strategy of employing BiNPs for Digoxin delivery is effective and enhances the expression levels of NIS proteins in transplanted tumors in nude mice.

Conclusion

In conclusion, this study presents a novel strategy for enhancing sensitization to RAI therapy by utilizing BiNPs as a multifunctional therapeutic platform. Current research on drug delivery systems for ATC redifferentiation is limited and predominantly focuses on organic nanoparticles, which are prone to rapid degradation and metabolism. Given the complexity of tumor pathogenesis, the efficacy of single therapeutic approaches is often inadequate. Furthermore, while some studies have explored the grafting of ligands for active targeting, these methods involve complex fabrication processes that are challenging to scale up for mass production.[30] In this study, glucose-modified BiNPs were synthesized in a single step, employing glucose as a surfactant to enhance drug utilization by leveraging the high glucose uptake characteristic of tumors, thereby improving the redifferentiation efficiency of digoxin. The high atomic number and excellent photothermal conversion efficiency of BiNPs facilitate both physical sensitization and PTT in the context of RAI treatment. Compared to other drug delivery systems, this approach is straightforward to synthesize and highly versatile, offering a promising solution to address the limitations associated with RAI therapy in the treatment of thyroid cancer.

Regarding the clinical translation potential of Bi@Digoxin, first, in terms of scalability, the next key step lies in overcoming the challenges of transitioning from simple laboratory synthesis to large-scale production processes that meet Good Manufacturing Practice standards. Second, at the regulatory approval level, more systematic standardized toxicology studies supporting long-term medication use must be conducted, ultimately requiring rigorous clinical trials to verify its safety and efficacy in patients. Addressing these issues will be crucial for advancing this nanoplatform into actual use for treating ATC.

Experimental Section

Materials and Reagents

The chemicals and reagents used were of analytical grade. Bismuth nitrate pentahydrate ($Bi(NO_3)_3{\cdot}5H_2O$, ≥ 99.99%), D-(+)-glucose ($C_6H_{12}O_6$), 1,2-propanediol (PPD, ≥ 99%), and borane-morpholine complex (C_4H_9NO- BH_3, ≥ 95%) was purchased from Aladdin's Reagent. RPMI 1640, penicillin/streptomycin, fetal bovine serum, and phosphate-buffered saline were purchased from sangon Biotech. NIS, GAPDH primary antibody was purchased from Proteintech, and Cleaved PARP primary antibody was purchased from Abcam. The Caspase-3/7 activity assay kit was purchased from Elabscience. Calcein/PI cell viability and cytotoxicity assay kit, ROS assay kit, and DNA damage assay kit were purchased from Beyotime.

Characterization

TEM imaging of nanoparticle samples was accomplished using JEM-F200 at an accelerating voltage of 200 kV (JEOL, Japan). XRD data were acquired on a SmartLab SE (Rigaku, Japan) diffractometer. UV-Vis-NIR absorption spectra and FT-IR spectra were measured at room temperature using a nanodrop 2000 UV-Vis-NIR spectrophotometer (Thermo Fisher Scientific, USA) and a Nicolet iS20 FT-IR spectrometer (Thermo Fisher Scientific, USA), respectively.

Synthesis of BiNPs

BiNPs were synthesized with reference to previously published methods with modifications.[31] PPD was used as a solvent, and Bi $(NO_3)_3 \cdot 5H_2O$ solution (485 mg, 4 mL) was magnetically stirred with D-(+)-glucose solution (10 g, 84 mL) in a water bath at 80 °C for 1h, and boranomorpholine (308 mg, 12 mL) was added for 60s to trigger the formation of nanoparticles. Pre-cooled 100 mL of deionized water was then added to the above reaction solution for quenching and the mixture was centrifuged at 8000 rpm for 1h and the supernatant removed. In order to remove excess reaction reagents or by-products, the precipitate was continued to be washed three times with deionized water and finally freeze-dried and stored at 4 °C.

Digoxin Loading and Release

3 mg of BiNPs powder was dispersed in 10 mL of deionized water, Digoxin was added in different ratios and the reaction was magnetically stirred at room temperature for 24 h. The suspension was centrifuged to discard the supernatant, and the precipitate was washed with deionized water to remove the free Digoxin, and the resultant drug-loaded Bi@Digoxin was placed in a refrigerator at 4 °C for storage. The supernatant was collected by centrifugation of 3 mg/mL Bi@Digoxin suspension before and after laser (808 nm, 1 W) irradiation, and the amount of drug released was calculated.

Cell Culture and in vitro Cytotoxicity

HUVEC were obtained from Wuhan Pricella Biotechnology Co., Ltd. 8505C were obtained from the Cell Bank of Type Culture Collection of the Chinese Academy of Sciences. Cells were cultured in RPMI 1640 medium containing 10% fetal bovine serum and 1% penicillin/streptomycin at 37 °C in a constant temperature, 5% CO_2 incubator. HUVEC and 8505C cells were inoculated into 96-well plates for adherent growth for 24 h. PBS suspensions containing different concentrations (0–100 μg/mL) of BiNPs were co-cultured with the cells for 24 h. Cell viability was detected by the CCK8 assay. 8505C cells were inoculated into 96-well plates for adherent growth for 24 h. PBS suspensions containing different concentrations (0–800 μCi/mL) of ^{131}I, 10 μg/mL BiNPs were co-cultured with the cells for 24 h. Cell viability was detected by CCK8 assay. 8505C cells were inoculated into 96-well plates for adherent growth for 24 h. PBS suspensions containing different concentrations (0–100 μg/mL, Unless otherwise specified, the concentration of free digoxin is invariably equivalent to that loaded in Bi@Digoxin) of Digoxin, Bi@Digoxin were co-cultivated with the cells for 4 h, respectively, and then washed off the uninternalized drug with PBS, and the culture was continued for 24h, and cell viability was detected by CCK8 method.

Cellular Uptake of BiNPs

Using PBS treatment as the control group. HUVEC and 8505C cells were inoculated into 6-well plates and grown on the wall for 24 h. BiNPs (20 μg/mL) were co-cultured with the cells for 4 h and then washed with PBS to remove the uninternalized drug, and the cells were collected for single-cell observation under bio-TEM system. HUVEC and 8505C cells were inoculated into 6-well plates for adherent growth for 24 h. BiNPs (20 μg/mL) were co-cultured with the cells for different times (1–24 h) and the uninternalized nanomaterials were washed away with PBS, and the cells were collected for detection of elemental Bi content by ICP-MS.

Western Blotting

8505C cells were inoculated in 6-well plates for adherent growth for 24 h. Five groups were set up with Control (PBS), BiNPs, Digoxin, Bi@Digoxin, Bi@Digoxin + NIR (BiNPs, Bi@Digoxin = 10 μg/mL). After co-culturing with the cells for 4 h, the uninternalized drug was washed away with PBS, and the laser (808 nm, 1 W) treated group was irradiated for 5 min, and the culture was continued for 24 h. Proteins were extracted from the cells for NIS expression analysis by Western blot, and the intensity of the bands was quantified by ImageJ software. 8505C cells were inoculated into 6-well plates for adherent growth for 24 h. Five groups were set up, namely: Control (PBS), BiNPs, ^{131}I, ^{131}I + BiNPs, ^{131}I + BiNPs + NIR (^{131}I = 400 μCi/mL, BiNPs = 10 μg/mL). The cells were incubated with the respective agents for 24 h, and the laser (808 nm, 1 W) treated group was irradiated for 5 min. Proteins were extracted from the cells by Western blot for Cleaved PARP expression analysis, and the intensity of the bands was quantified by ImageJ software. 8505C cells were

inoculated in 6-well plates for adherent growth for 24 h. Three groups were set up with Control (PBS), Selumetinib, Bi@Digoxin (Selumetinib = 10 μM, Bi@Digoxin = 10 μg/mL). After co-culturing with the cells for 4 h, the uninternalized drug was washed away with PBS, and the culture was continued for 24 h. Proteins were extracted from the cells for NIS expression analysis by Western blot.

Caspase 3/7 Activity

8505C cells were inoculated into 96-well plates for adherent growth for 24 h. Five groups were set up, namely: Control (PBS), BiNPs, ^{131}I, ^{131}I + BiNPs, ^{131}I + BiNPs + NIR (^{131}I = 400 μCi/mL, BiNPs = 10 μg/mL). The cells were incubated with the respective agents for 24 h, and the laser (808 nm, 1 W) treated group was irradiated for 5 min. The cells were treated with Caspase-3/7 activity assay kit, and the signal values were measured at 405 nm wavelength using a microplate reader. All results were normalized as fold changes relative to the control group.

Iodine Intake

8505C cells were inoculated in 12-well plates for adherent growth for 24 h. Three groups were set up with Control (PBS), Digoxin, and Bi@Digoxin (Bi@Digoxin = 10 μg/mL), respectively, and the cells were co-cultured with each other for 4 h. The uninternalized drug was washed away with PBS, and the culture was continued for 24 h. Cells were incubated with 2 μCi Na ^{125}I for 45 min at 37 °C with or without the competitive NIS inhibitor sodium perchlorate (300 μM), to control NIS-specific uptake. Uninternalized ^{125}I was then washed away and lysed with 500 μL formic acid. The radioactivity was measured in the cell lysates using a gamma radioimmunoassay counter (ANHUI USTC ZONKIA Scientific Instruments Co., Ltd., Anhui, China). All measured values have been deducted from the background. The radioactivity is expressed in counts per minute (cpm)/10^6 cells. Three groups were set up with Control (PBS), Selumetinib, Bi@Digoxin (Selumetinib = 10 μM, Bi@Digoxin = 10 μg/mL). After co-culturing with the cells for 4 h, the uninternalized drug was washed away with PBS, and the culture was continued for 24 h. Subsequent procedures were consistent with the aforementioned protocol.

Fluorescent Staining

8505C cells were inoculated in 6-well plates and grown in adherence for 24 h. Five groups were set up, namely Control (PBS), ^{131}I, ^{131}I + BiNPs, ^{131}I + Bi@Digoxin, ^{131}I + Bi@Digoxin + NIR (^{131}I = 400 μCi/mL, BiNPs, Bi@Digoxin = 10 μg/mL). After co-culturing with cells for 4 h, the uninternalized drug was washed away with PBS, ^{131}I was added, and the laser (808 nm, 1 W) treated group was irradiated for 5 min, and continued to be cultured for 24 h. Fluorescent staining of Calcein AM/PI, DCFH-DA, and γ-H2AX was carried out, respectively, and placed under the fluorescence microscope for observation. The fluorescence intensity of ROS was quantitatively analyzed by zymography. γ-H2AX was quantitatively analyzed by ImageJ software.

Cell Clone Formation

8505C cells were inoculated into 6-well plates for adherent growth for 24 h. Five groups were set up, Control (PBS), ^{131}I, ^{131}I + BiNPs, ^{131}I + Bi@Digoxin, ^{131}I + Bi@Digoxin + NIR (^{131}I = 10 μCi/mL, BiNPs, Bi@Digoxin = 10 μg/mL). After 4 h of co-culture with the cells, the uninternalized drug was washed away with PBS, ^{131}I was added, and the laser (808 nm, 1 W) treated group was irradiated for 5 min, and the culture was continued for 24 h. The cells were trypsin digested, counted, and spread in six-well plates at 1×10^3 cells per well. After 14 days of drug treatment, the formed colonies were washed with PBS and fixed with 4% paraformaldehyde and stained by adding 0.4% crystal violet solution. Then the percentage of clone formation and survival fraction were calculated.

In vivo Biocompatibility Validation

BiNPs (20 mg/kg) were injected into the tail vein of mice, and mice treated with PBS were used as controls. Fresh blood was extracted for routine blood index tests and serum biochemistry. In addition, major organs were collected and then immersed in 4% paraformaldehyde for further staining with H&E. Intact blood samples were collected from healthy mice and incubated with BiNPs at different concentrations; PBS group was the negative control and H_2O group was the positive control. 5 h later, the supernatant was collected by centrifugation, and the absorbance was measured by an

enzyme marker at 570 nm. BiNPs (20 mg/kg) were injected into the tail vein of mice. At predetermined time points, 15 μL of mouse blood was collected, and the Bi element content was measured using ICP. For the in vivo distribution experiment, after intravenous injection of the same dose of dispersion, the mice were sacrificed after 12 hours. Their major organs, including the heart, liver, spleen, lungs, and kidneys, were dissected, and the Bi element content was measured using ICP to calculate its distribution in the body.

Establishment of Animal Models and in vivo Therapeutic Evaluation

A mouse tumor-bearing model was established by injecting 5×10^6 8505C cells into the right axilla of female Balb/c-nu. When the tumor size reached approximately 100 mm^3, the mice were divided into different groups for treatment. Since tumor volume can affect treatment efficacy, a randomized block design was employed to group mice based on tumor volume, ensuring similarity in tumor size across different groups. Balb/c-nu was randomized into five groups: control (PBS), ^{131}I, ^{131}I + BiNPs, ^{131}I + Bi@Digoxin, and ^{131}I + Bi@Digoxin + NIR (^{131}I = 800 μCi, BiNPs, Bi@Digoxin = 10 mg/kg). Given that RAI is suitable for eliminating residual cancer cells while PTT is appropriate for treating superficial solid tumors, we adopted two distinct drug delivery routes to achieve synergistic therapeutic effects while confining the radiosensitizing to the tumor, thereby effectively reducing side effects. Mice were treated with intravenous injection of ^{131}I via the tail vein, intratumoral injection of the other drugs, and exposure to an 808 nm laser at 1 W/cm^2 for 10 min. Tumor size and body weight were measured every 2 days, and the mice were executed after 14 days, and the tumor tissues were extracted and then subjected to pathological examination. Comparison of tumor redifferentiation effect: Balb/c-nu was randomly divided into three groups, Control (PBS), Digoxin, Bi@Digoxin (Bi@Digoxin = 10 mg/kg, Digoxin concentration equal to Digoxin loaded in Bi@Digoxin), and intratumorally injected with the drug. Mice were put to death after 14 days, and the tumor was extracted tissues, followed by NIS immunohistochemical staining.

Statistical Analysis

All the experiments were repeated at least three times. Data were expressed as mean ± standard deviation (SD). Student's *t*-test performed comparisons for two groups, and ANOVA for multiple groups using GraphPad Prism 8. *$p < 0.05$ was considered to be statistically significant. **$p < 0.01$, ***$p < 0.001$ and ****$p < 0.0001$ were highly statistically significant between the groups.

Data Sharing Statement

Data of this study will be made available upon reasonable request from the corresponding authors.

Ethics Approval and Informed Consent

All experimental procedures were conducted in accordance with institutional guidelines for the care and use of laboratory animals and protocols, which were approved by Health Science Center of Xi'an Jiaotong University (Granted Number: XJTUAE 2024-2510).

Author Contributions

All authors made a significant contribution to the work reported, whether that is in the conception, study design, execution, acquisition of data, analysis and interpretation, or in all these areas; took part in drafting, revising or critically reviewing the article; gave final approval of the version to be published; have agreed on the journal to which the article has been submitted; and agree to be accountable for all aspects of the work.

Funding

This work was supported by the Shaanxi Medical-Industrial Fusion High-end Medical Equipment Common Technology R&D Platform 3-2 Ultra-high Resolution Second Imaging PET Common Technology R&D Sub-platform (2023GXJS-01-7).

Disclosure

The authors declare no conflicts of interest in this work.

References

1. Cabanillas ME, McFadden DG, Durante C. Thyroid cancer. *Lancet*. 2016;388(10061):2783–2795. doi:10.1016/s0140-6736(16)30172-6
2. Califano I, Smulever A, Jerkovich F, Pitoia F. Advances in the management of anaplastic thyroid carcinoma: transforming a life-threatening condition into a potentially treatable disease. *Rev Endocr Metab Disord*. 2024;25(1):123–147. doi:10.1007/s11154-023-09833-1
3. Smallridge RC, Copland JA. Anaplastic thyroid carcinoma: pathogenesis and emerging therapies. *Clin Oncol*. 2010;22(6):486–497. doi:10.1016/j.clon.2010.03.013
4. Zheng L, Li L, He Q, et al. Response to immunotherapy in a patient with anaplastic thyroid cancer: a case report. *Medicine*. 2021;100(32):e26138. doi:10.1097/md.0000000000026138
5. Ze Y, Shao F, Feng X, et al. Effect of liver dysfunction on outcome of radioactive iodine therapy for Graves' disease. *BMC Endocr Disord*. 2022;22(1):319. doi:10.1186/s12902-022-01242-w
6. Cao H, Shangguan L, Zhu H, et al. Prognostic analysis of 131I efficacy after papillary thyroid carcinoma surgery based on CT radiomics. *J Clin Endocrinol Metab*. 2024;109(12):3036–3045. doi:10.1210/clinem/dgae364
7. Li Q, Zhang L, Lang J, et al. Lipid-peptide-mRNA nanoparticles augment radioiodine uptake in anaplastic thyroid cancer. *Adv Sci*. 2023;10(3):e2204334. doi:10.1002/advs.202204334
8. Huang S, Wu Y, Li C, et al. Tailoring morphologies of mesoporous polydopamine nanoparticles to deliver high-loading radioiodine for anaplastic thyroid carcinoma imaging and therapy. *Nanoscale*. 2021;13(35):15021–15030. doi:10.1039/d1nr02892h
9. Kassis AI. Therapeutic radionuclides: biophysical and radiobiologic principles. *Semin Nucl Med*. 2008;38(5):358–366. doi:10.1053/j.semnuclmed.2008.05.002
10. Tesselaar MH, Crezee T, Swarts HG, et al. Digitalis-like compounds facilitate non-medullary thyroid cancer redifferentiation through intracellular Ca2+, FOS, and autophagy-dependent pathways. *Mol Cancer Ther*. 2017;16(1):169–181. doi:10.1158/1535-7163.Mct-16-0460
11. Tesselaar MH, Crezee T, Schuurmans I, et al. Digitalislike compounds restore hNIS expression and iodide uptake capacity in anaplastic thyroid cancer. *J Nucl Med*. 2018;59(5):780–786. doi:10.2967/jnumed.117.200675
12. Groen-Wijnberg M, van Dijk J, Krauwinkel W, et al. Pharmacokinetic interactions between mirabegron and metformin, warfarin, digoxin or combined oral contraceptives. *Eur J Drug Metab Pharmacokinet*. 2017;42(3):417–429. doi:10.1007/s13318-016-0350-5
13. Dessale M, Mengistu G, Mengist HM. Nanotechnology: a promising approach for cancer diagnosis, therapeutics and theragnosis. *Int J Nanomed*. 2022;17:3735–3749. doi:10.2147/ijn.S378074
14. Fröhlich E, Wahl R. Nanoparticles: promising auxiliary agents for diagnosis and therapy of thyroid cancers. *Cancers*. 2021;13(16):4063. doi:10.3390/cancers13164063
15. Badrigilan S, Heydarpanahi F, Choupani J, et al. A review on the biodistribution, pharmacokinetics and toxicity of bismuth-based nanomaterials. *Int J Nanomed*. 2020;15:7079–7096. doi:10.2147/ijn.S250001
16. Sun H, Li H, Harvey I, Sadler PJ. Interactions of bismuth complexes with metallothionein(II). *J Biol Chem*. 1999;274(41):29094–29101. doi:10.1074/jbc.274.41.29094
17. Kempson I. Mechanisms of nanoparticle radiosensitization. *Wiley Interdiscip Rev Nanomed Nanobiotechnol*. 2021;13(1):e1656. doi:10.1002/wnan.1656
18. Xue S, Jiao J, Miao S, et al. Lipid-coated bismuth nanoflower as the thermos-radio sensiti for therapy of lung metastatic breast cancer: preparation, optimisation, and characterisation. *IET Nanobiotechnol*. 2022;16(9):305–315. doi:10.1049/nbt2.12097
19. Shahbazi MA, Faghfouri L, Ferreira MPA, et al. The versatile biomedical applications of bismuth-based nanoparticles and composites: therapeutic, diagnostic, biosensing, and regenerative properties. *Chem Soc Rev*. 2020;49(4):1253–1321. doi:10.1039/c9cs00283a
20. Kong T, Zeng J, Wang X, et al. Enhancement of radiation cytotoxicity in breast-cancer cells by localized attachment of gold nanoparticles. *Small*. 2008;4(9):1537–1543. doi:10.1002/smll.200700794
21. Qi QR, Tian H, Yue BS, Zhai BT, Zhao F. Research progress of SN38 drug delivery system in cancer treatment. *Int J Nanomed*. 2024;19:945–964. doi:10.2147/ijn.S435407
22. Oh JM, Ahn BC. Molecular mechanisms of radioactive iodine refractoriness in differentiated thyroid cancer: impaired sodium iodide symporter (NIS) expression owing to altered signaling pathway activity and intracellular localization of NIS. *Theranostics*. 2021;11(13):6251–6277. doi:10.7150/thno.57689
23. Zhang J, Zhao A, Jia X, et al. Sinomenine hydrochloride promotes TSHR-dependent redifferentiation in papillary thyroid cancer. *Int J Mol Sci*. 2022;23(18):10709. doi:10.3390/ijms231810709
24. Gerken LRH, Gogos A, Starsich FHL, et al. Catalytic activity imperative for nanoparticle dose enhancement in photon and proton therapy. *Nat Commun*. 2022;13(1):3248. doi:10.1038/s41467-022-30982-5
25. Liu Z, Xie F, Xie J, et al. New-generation photosensitizer-anchored gold nanorods for a single near-infrared light-triggered targeted photodynamic-photothermal therapy. *Drug Deliv*. 2021;28(1):1769–1784. doi:10.1080/10717544.2021.1960923
26. Kim IG, Kim JS, Lee JH, Cho EW. Genistein decreases cellular redox potential, partially suppresses cell growth in HL-60 leukemia cells and sensitizes cells to γ-radiation-induced cell death. *Mol Med Rep*. 2014;10(6):2786–2792. doi:10.3892/mmr.2014.2611
27. Yu D, Feng Y, Jiang Z, et al. The role of human antigen R (HuR) in modulating proliferation, senescence and radiosensitivity of skin cells. *Exp Ther Med*. 2022;24(3):566. doi:10.3892/etm.2022.11503
28. Wang Y, Niu K, Shi Y, et al. A review: targeting UBR5 domains to mediate emerging roles and mechanisms - chance or necessity? *Int J Surg*. 2024;110(8):4947–4964. doi:10.1097/js9.0000000000001541
29. Shi Y, Wang J, Huang G, et al. A novel epithelial-mesenchymal transition gene signature for the immune status and prognosis of hepatocellular carcinoma. *Hepatol Int*. 2022;16(4):906–917. doi:10.1007/s12072-022-10354-3
30. Tran S, DeGiovanni PJ, Piel B, Rai P. Cancer nanomedicine: a review of recent success in drug delivery. *Clin Transl Med*. 2017;6(1):44. doi:10.1186/s40169-017-0175-0
31. Brown AL, Naha PC, Benavides-Montes V, Litt HI, Goforth AM, Cormode DP. Synthesis, X-ray opacity, and biological compatibility of ultra-high payload elemental bismuth nanoparticle X-ray contrast agents. *Chem Mater*. 2014;26(7):2266–2274. doi:10.1021/cm500077z